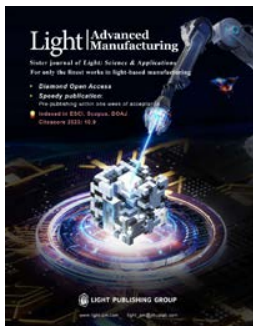


Accepted Article Preview: Published ahead of advance online publication



## Light focusing and additive manufacturing through highly scattering media using upconversion nanoparticles

Qianyi Zhang, Antoine Boniface, Virendra K. Parashar, Viola Sgarminato, Jorge Madrid-Wolff, Martin A. M. Gijs, and Christophe Moser

Cite this article as: Qianyi Zhang, Antoine Boniface, Virendra K. Parashar, Viola Sgarminato, Jorge Madrid-Wolff, Martin A. M. Gijs, and Christophe Moser. Light focusing and additive manufacturing through highly scattering media using upconversion nanoparticles. *Light: Advanced Manufacturing* accepted article preview 14 February 2025; doi: 10.37188/lam.2025.021

This is a PDF file of an unedited peer-reviewed manuscript that has been accepted for publication. LAM is providing this early version of the manuscript as a service to our customers. The manuscript will undergo copyediting, typesetting and a proof review before it is published in its final form. Please note that during the production process errors may be discovered which could affect the content, and all legal disclaimers apply.

Received: 11 April 2024 Revised: 13 January 2025 Accepted: 13 February 2025; Accepted article preview online 14 February 2025

1 **Light focusing and additive manufacturing through highly**  
2 **scattering media using upconversion nanoparticles**

3 **Qianyi Zhang<sup>1</sup>, Antoine Boniface<sup>1</sup>, Virendra K. Parashar<sup>2</sup>, Viola Sgarminato<sup>1</sup>, Jorge**  
4 **Madrid-Wolff<sup>1</sup>, Martin A. M. Gijs<sup>2</sup>, and Christophe Moser<sup>1,\*</sup>**

5 <sup>1</sup>Laboratory of Applied Photonics Devices, School of Engineering, Institute of Electrical and  
6 Micro Engineering, Ecole Polytechnique Fédérale de Lausanne, Lausanne, Switzerland

7 <sup>2</sup>Laboratory of Microsystems LMIS2, School of Engineering, Institute of Electrical and  
8 Micro Engineering, Ecole Polytechnique Fédérale de Lausanne, Lausanne, Switzerland

9 <sup>\*</sup>To whom correspondence should be addressed. e-mail: christophe.moser@epfl.ch

**10 Abstract**

11 Light-based additive manufacturing holds great potential in the field of bioprinting due to its  
12 exceptional spatial resolution, enabling the reconstruction of intricate tissue structures.  
13 However, printing through biological tissues is severely limited due to the strong optical  
14 scattering within the tissues. The propagation of light is scrambled to form random speckle  
15 patterns, making it impossible to print features at the diffraction-limited size with  
16 conventional printing approaches. The poor tissue penetration depth of ultra-violet or blue  
17 light, which is commonly used to trigger photopolymerization, further limits the fabrication  
18 of high cell-density tissue constructs. Recently, several strategies based on wavefront shaping  
19 have been developed to manipulate the light and refocus it inside scattering media to a  
20 diffraction-limited spot. In this study, we present a high-resolution additive manufacturing  
21 technique using upconversion nanoparticles and a wavefront shaping method that does not  
22 require measurement from an invasive detector, i.e., it is a non-invasive technique.  
23 Upconversion nanoparticles convert near-infrared light to ultraviolet and visible light. The  
24 ultraviolet light serves as a light source for photopolymerization and the visible light as a  
25 guide star for digital light shaping. The incident light pattern is manipulated using the  
26 feedback information of the guide star to focus light through the tissue. In this way, we  
27 experimentally demonstrate that near-infrared light can be non-invasively focused through a  
28 strongly scattering medium. By exploiting the optical memory effect, we further demonstrate  
29 micro-meter resolution additive manufacturing through highly scattering media such as a  
30 300- $\mu\text{m}$ -thick chicken breast. This study provides a concept of high-resolution additive  
31 manufacturing through turbid media with potential application in tissue engineering.

32

33 **Keywords:** additive manufacturing; hydrogels; light-based additive manufacturing;  
34 upconversion nanoparticles; bioprinting; wavefront shaping; scattering

## 35 Introduction

36 Bioprinting, a cutting-edge technology that merges biology and additive manufacturing, has  
37 revolutionized the field of tissue engineering<sup>1,2</sup>. This innovative approach allows for the  
38 precise deposition of biomaterials, cells, and growth factors to fabricate complex, functional  
39 tissues and organs<sup>3-5</sup>. As a result, bioprinting has opened new frontiers in tissue engineering,  
40 offering potential solutions for broad applications including disease modeling<sup>6,7</sup>, drug  
41 testing<sup>8,9</sup>, and regenerative medicine<sup>1,10</sup>. Common bioprinting methods include inkjet  
42 printing<sup>11</sup>, extrusion-based printing<sup>12</sup>, laser-induced forward transfer<sup>13</sup>, and light-based  
43 additive manufacturing<sup>14-16</sup>. Laser- and light-based additive manufacturing has the advantage  
44 of high resolution (~1  $\mu\text{m}$ ) compared to that of nozzle-based techniques such as inkjet  
45 printing and extrusion-based printing (~100  $\mu\text{m}$ )<sup>17</sup>. Bioprinted implants typically involve a  
46 surgical intervention for the implantation<sup>18,19</sup> or for direct in-situ biofabrication at the exposed  
47 site<sup>20,21</sup>, which poses inherent challenges and risks.

48 To address these limitations, non-invasive and minimally invasive bioprinting has emerged as  
49 a powerful solution by offering the possibility of creating functional biological constructs  
50 bypassing invasive surgical procedures<sup>22-25</sup>. Light-based additive manufacturing, which  
51 employs light to solidify resins without the need for direct material deposition, is particularly  
52 well positioned compared to other minimally invasive bioprinting techniques thanks to light  
53 and its possibility of delivering energy through tissues. More precisely, the light energy is  
54 sent through the tissue to initiate photopolymerization of the injected bio-ink and transform it  
55 into desired structures. Light transport in biological tissues is determined by their absorption  
56 and scattering properties. Ultra-violet (UV) or blue light, which is commonly used in  
57 photopolymerization, shows poor tissue penetration depth and is not favorable for non-  
58 invasive bioprinting. The near-infrared (NIR) window with a wavelength ranging from 650 to  
59 1350 nm, offers deeper penetration into biological tissues with less significant attenuation  
60 because of its longer wavelength (less scattering) and the lack of absorption from biological  
61 molecules<sup>26</sup>. Therefore, NIR light is well-suited for *in vivo* imaging<sup>27-30</sup> and therapeutic  
62 applications<sup>30-32</sup> that require light to reach target areas deep within the body. It can induce  
63 photopolymerization via two-photon absorption<sup>33</sup> or upconverting process<sup>34</sup> and has already  
64 been demonstrated in non-invasive additive manufacturing<sup>22-24</sup>.

65 Although NIR light is transmitted more efficiently through tissues, scattering still scrambles  
66 the propagating light field to form complex speckle patterns, preventing focusing the light to  
67 a tiny spot for a well-confined delivery of light energy. This greatly impacts the resolution

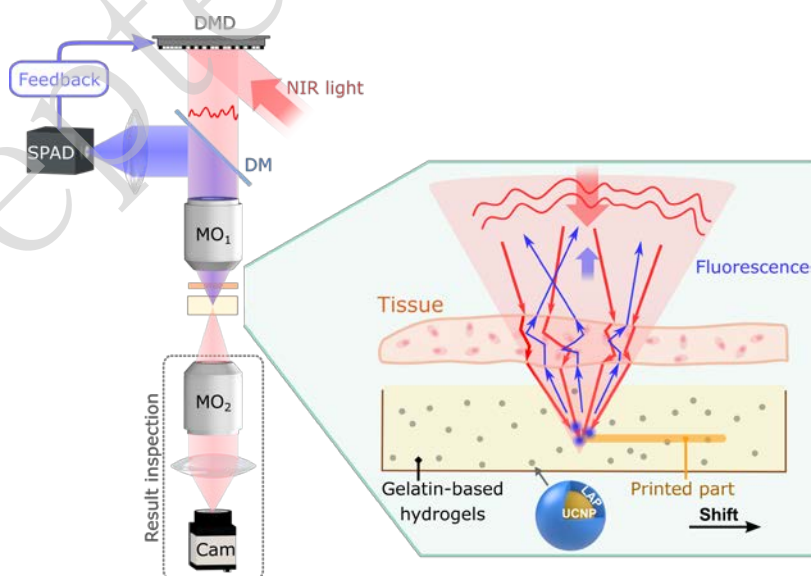
68 (from 1  $\mu\text{m}$  in the absence of tissue to tens or hundreds  $\mu\text{m}$  depending on tissue properties  
69 and thickness) and the fidelity of non-invasive printing<sup>22,24</sup>. In the field of optical imaging,  
70 several strategies based on wavefront shaping have been developed to manipulate the light  
71 and refocus it through scattering media to a diffraction-limited spot<sup>35-41</sup>. These techniques  
72 utilize feedback signals obtained behind the scattering media to spatially modulate the input  
73 light in phase and amplitude. For non-invasive light focusing, fluorescent or acoustics signals  
74 emanating inside or behind the scattering medium can be measured from the same side as the  
75 light delivery<sup>38,39,41</sup>. However, these techniques only provide the wavefront information of  
76 one target location at a time, and it is time-consuming to refocus at each voxel to be printed.  
77 Fortunately, the scattered optical field preserves a certain degree of correlation, which is  
78 commonly referred to as the optical memory effect<sup>42,43</sup>. When an input wavefront reaching a  
79 scattering medium is shifted (or tilted) within a certain distance (or angle), the output  
80 wavefront propagating through the medium is equally shifted (or tilted). In thick biological  
81 media, where scattering is anisotropic (anisotropic factor  $g$  usually ranges from 0.9 to 0.98<sup>26</sup>),  
82 the range of tilt/tilt memory effect becomes minimal (50- $\mu\text{m}$ -thick tissues around 3-8  $\text{mrad}$ <sup>44</sup>)  
83 but strong shift/shift correlations are still observed<sup>43</sup>. In this way, the focal spot can be shifted  
84 through the scattering medium before it becomes too dim so that the next focusing  
85 optimization can be generated in a time-efficient manner<sup>45</sup>. The scattering effect of the tissue  
86 is thus corrected during the printing using sparse focusing, which significantly speeds up the  
87 printing as compared with optimizing at every subsequent spot.

88 In this study, we develop a micro-meter resolution additive manufacturing technique through  
89 a highly scattering medium assisted by upconversion nanoparticles (UCNPs). As the UCNP  
90 generates fluorescence of different wavelengths under the illumination of NIR light, it acts  
91 not only as a secondary UV source for photopolymerization but can also be used as a guide  
92 star for the feedback loop to refocus light through the scattering media. Then, the focal spot is  
93 scanned through the scattering medium using sparse focusing. Based on this technique, we  
94 are able to print high-resolution (2  $\mu\text{m}$ ) structures through a holographic diffuser and a  
95 chicken tissue of thickness 300  $\mu\text{m}$ . These results demonstrate high-resolution additive  
96 manufacturing through strongly scattering media and suggest potential applications in non-  
97 invasive biomedicine.

98

## 99 **Results**

100 We designed our non-invasive additive manufacturing system based on wavefront shaping, as  
 101 illustrated in Fig. 1. A NIR beam at 976 nm is first modulated in amplitude by a digital  
 102 micro-mirror device (DMD) and directed through a scattering medium (holographic diffuser  
 103 or chicken tissue) into the resin. The resin contains hydrogel monomers of gelatin  
 104 methacryloyl (gelMA) and UCNPs coated with the UV light photoinitiator lithium phenyl-  
 105 2,4,6-trimethylbenzoyl-phosphinate (LAP). The synthesized UCNPs are highly crystalline  
 106 and show hexagonal morphology, with an average particle size of  $\sim 10$  nm (Fig. S1). UCNPs  
 107 (positive) are coated with LAP (negative) through electrostatic interaction. This coating is  
 108 verified by Fourier transform infrared (FTIR) and Zeta potential analysis (Fig. S2). UCNPs  
 109 emit UV and visible fluorescence under the illumination of 976 nm light. The visible  
 110 fluorescence ( $440 \text{ nm} < \lambda < 550 \text{ nm}$ ), which is not absorbed by LAP, is back-scattered by the  
 111 scattering medium and epi-detected by a single-photon avalanche diode (SPAD), providing  
 112 the feedback signal for the optimization of the spatial light modulation (binary DMD pattern).  
 113 Then, the optimized DMD pattern is displayed and refocuses the NIR light through the  
 114 scattering medium to a diffraction-limited spot within the resin, which is shifted together with  
 115 the scattering medium to induce photopolymerization along the designed path. After a lateral  
 116 shift of the sample determined by the size of the memory effect (here around  $5 \mu\text{m}$ ), the  
 117 DMD pattern is re-optimized to focus light again and this scanning process is repeated until  
 118 the printed part is complete. The resulting spatial distribution of the NIR light at the focal  
 119 plane is inspected by a camera placed on the distal side of the sample, for observation  
 120 purposes only.



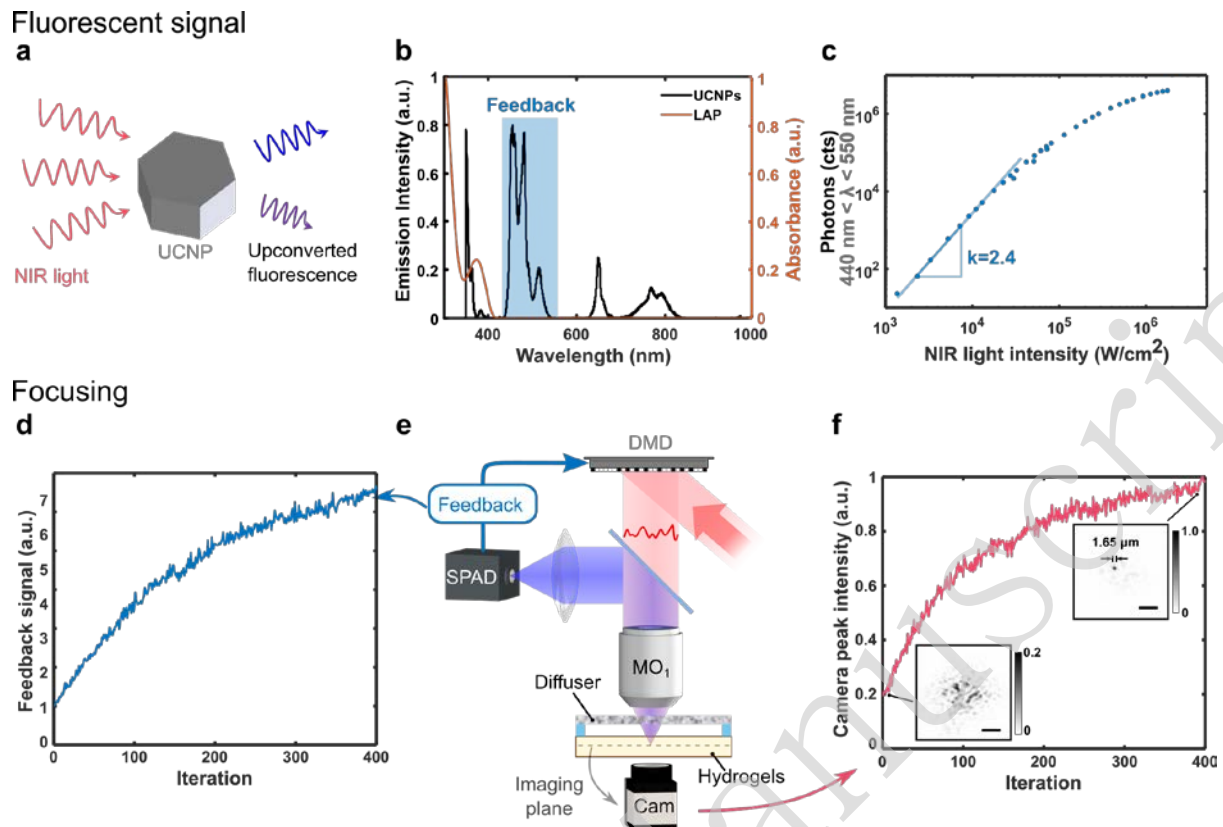
121

122 **Fig. 1** Schematic figure of high-resolution non-invasive additive manufacturing using UCNPs that are coated  
 123 with the photoinitiator LAP. The NIR beam is modulated by the DMD to compensate for the scattering and

124 focus the light through the tissue down to a diffraction-limited spot. The resin contains UCNPs that convert NIR  
125 light to UV and visible fluorescence, acting as the secondary UV source for inducing the photopolymerization of  
126 the hydrogels and as a guide star for wavefront shaping. By laterally shifting the sample across the print  
127 geometry, micro-meter resolution features can be printed through the tissue. DM: dichroic mirror. MO:  
128 microscope objective. Cam: camera.

129

130 The focusing process using the upconverted fluorescence as feedback is shown in Fig. 2.  
131 UCNPs convert NIR light to UV and visible light (Fig. 2a). The latter conveys information  
132 about the NIR speckle pattern within the resin. Fig. 2b shows the emission spectrum of  
133 UCNPs illuminated by 976 nm light and the absorption spectrum of the photoinitiator LAP.  
134 The emission peaks at 350 and 360 nm fall within the absorption band of LAP, suggesting  
135 that it is mainly absorbed by the LAP coating and contributes to photopolymerization. The  
136 rest of the fluorescence can be partially detected in reflection thanks to its isotropic emission.  
137 Upconverted fluorescence in the wavelength range of  $440 \text{ nm} < \lambda < 550 \text{ nm}$  is experimentally  
138 chosen as the feedback for the following consideration. The upconversion process to a high-  
139 energy photon involves multi-photon absorption, resulting in a nonlinear luminescence  
140 process. Each fluorescence peak corresponds to a certain nonlinearity parameter  $n$ , which can  
141 be understood as the number of NIR photons absorbed required to emit a photon of higher  
142 energy than the incident NIR photons. Due to the saturation of the excited energy states, the  
143 nonlinearity is experimentally experienced only at low light intensity. In the focusing process,  
144 signals generated from a high nonlinearity conversion are preferred because of their faster  
145 converging speed<sup>38,46,47</sup>. However, this signal only occurs at low intensity and shorter  
146 wavelength<sup>48</sup> and thus there is a balance between non-linearity and signal intensity since a  
147 higher photon count enables a faster collection and speeds up the focusing process.  
148 Upconverted fluorescence in this wavelength range is chosen because it covers most of the  
149 photons from visible emission and preserves a high average non-linearity. The total  
150 fluorescence is measured by the SPAD at different NIR intensities and plotted in the log scale  
151 (Fig. 2c). The NIR intensities are calculated by the laser power measured before the  
152 illumination objective divided by the beam size at the focal plane, and the transmission of this  
153 objective (~67% at 976 nm) is not taken into account. According to the definition, the slope  
154 of the curve in the log scale represents the nonlinear parameter  $n$ . The total fluorescent signal  
155 collected displays a slope of 2.4 at a lower intensity and a decreased nonlinearity at a higher  
156 intensity.



157

158 **Fig. 2** Focusing process based on the nonlinear fluorescent feedback. **a** Schematic diagram of the upconverting  
 159 process. **b** Emission spectrum of UCNPs (black) under 976 nm light illumination and absorption spectrum of the  
 160 photoinitiator LAP (orange). The wavelength band highlighted in blue represents the range of upconverted  
 161 fluorescence collected as the feedback. (a.u.= arbitrary units). **c** Fluorescent feedback versus NIR light intensity  
 162 in the log scale. The slope represents the nonlinearity parameter  $n$ . **d** Power-corrected feedback signal during the  
 163 iterative optimization. **e** Experimental setup for non-invasive focusing. A holographic diffuser is used in this  
 164 experiment. **f** Peak intensity of the NIR patterns inspected by the camera during the optimization. Insets show  
 165 the NIR patterns at the first and the final iteration. Full width at half maximum (FWHM) of the focal spot, 1.65  
 166  $\mu\text{m}$ . Scale bars, 10  $\mu\text{m}$ .

167 Because of the low upconversion efficiency of UCNPs, the total fluorescence is detected by a  
 168 single-pixel detector to ensure a good signal-to-noise ratio (Fig. 2e), at the expense of a loss  
 169 of spatial information of the speckle. As already demonstrated<sup>38,46,49</sup>, optimizing a nonlinear  
 170 spatially integrated signal enables blind focusing behind a scattering layer through iterative  
 171 optimization. By maximizing the total fluorescent signal, the light tends to redistribute the  
 172 energy to one single spot rather than over several grains of a speckle thanks to the nonlinear  
 173 fluorescence behavior at the chosen NIR intensity. Note that, we have no control over the  
 174 position of the focal spot, which can be at any hot spot of the speckle illuminating the resin.  
 175 In most of the previous research works<sup>38,46,47,49</sup>, the light is modulated in phase with a liquid  
 176 crystal-based spatial light modulator (LC-SLM), which does not change the light power after



177 the modulation. In this work, however, a DMD is implemented because of its faster operation  
 178 (~20 kHz) compared to that of LC-SLM (~60 Hz). Therefore, the light is modulated only in  
 179 amplitude, resulting in pattern-dependent output power. The fluorescence signal is also  
 180 dependent on the number of pixels on the DMD with the “ON” state, which does not  
 181 necessarily result in a focal spot. Therefore, the fitness function  $f(x)$  for a DMD pattern  $\mathbf{Z}$  is  
 182 calculated as:

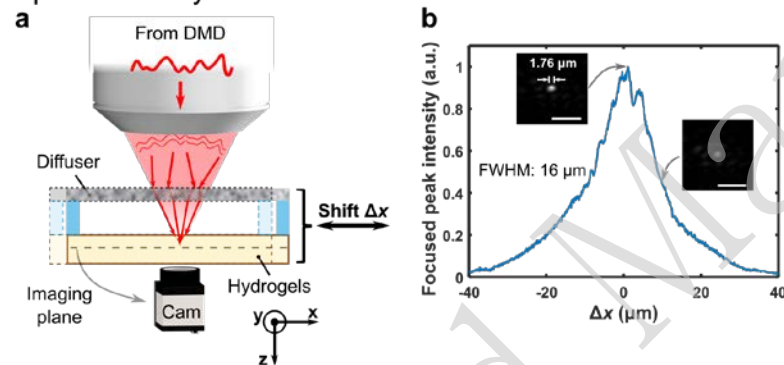
$$f(\mathbf{Z}) = \frac{P_{\text{fluo}}}{I_{\text{DMD}} \odot \mathbf{Z}} \quad (1)$$

183  $P_{\text{fluo}}$  is the total fluorescent signal resulting from this DMD pattern.  $I_{\text{DMD}} \odot \mathbf{Z}$  is the element-  
 184 wise product of NIR light distribution on DMD (Fig. S3) and the DMD pattern  $\mathbf{Z}$ , which  
 185 gives the light power of this pattern before the illumination objective. By maximizing this  
 186 fitness function, the iterative algorithm tries to find the DMD pattern that excites more  
 187 fluorescence per NIR light power, which compensates for the effect of amplitude modulation.  
 188 In the iterative optimization, we adopted separable natural evolution strategies<sup>50</sup> (SNES) to  
 189 increase the converging speed of the global search and shorten the optimization time.  
 190 Multiple pixels are encoded with a number between 0 and 1 (Fig. S4a) to eliminate the drastic  
 191 change between pixels in the binary amplitude modulation<sup>50</sup>. The focusing process is  
 192 operated at low NIR power (average intensity of  $\sim 3 \times 10^3 \text{ W/cm}^2$ ): the nonlinearity parameter  
 193  $n$  is large, resulting in a faster converging speed; the light dose is much lower than the  
 194 photopolymerization threshold so that it does not induce photopolymerization. The camera  
 195 placed on the other side of the sample is only used for imaging the NIR pattern. Because the  
 196 focal spot can converge at any position of the resin volume illuminated by the speckle, the  
 197 resin is contained in a rectangular capillary with an inner thickness of 20  $\mu\text{m}$  to limit the  
 198 position of the focal spot along the optical axis, making it easier for the alignment of the  
 199 imaging system (see Section S5, Supplementary Information). By maximizing the feedback  
 200 signal mentioned above (Fig. 2d), the peak intensity on the image of the NIR pattern  
 201 increases with the iteration (Fig. 2f), leading to only one sharp spot behind the diffuser. The  
 202 diffraction limit of this system is determined by the numerical aperture (NA). In this study,  
 203 we use an NA 0.40 objective to focus the light after DMD projection. The NA of this system  
 204 is  $\sim 0.40$  after passing through the scattering layer because both the holographic diffuser and  
 205 the tissue are anisotropic scattering media. Therefore, the theoretical diffraction limit is  $d =$   
 206  $\lambda/\text{NA} = 1.22 \mu\text{m}$ . FWHM of the focal spot measured from 5 different samples is  $1.65 \pm 0.13$   
 207  $\mu\text{m}$ . It is slightly larger than the theoretical diffraction limit, which is mainly because of the

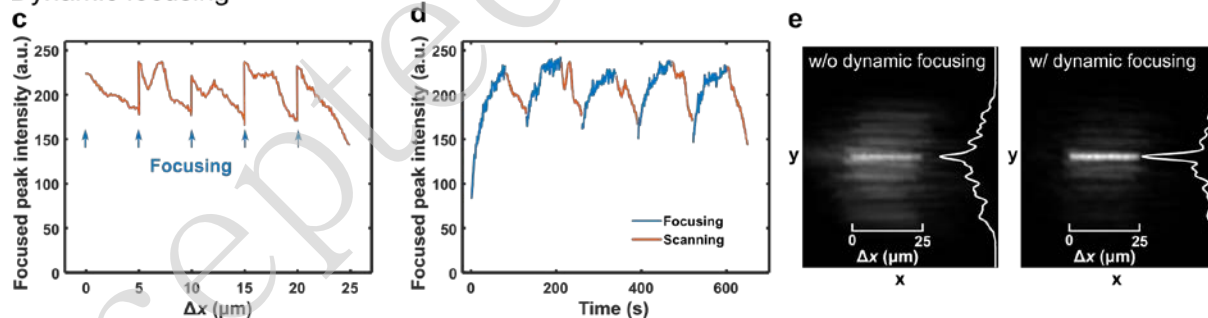
208 following reasons. First, the modulated beam is slightly smaller than the back aperture of the  
 209 objective in order to use the full pattern of the DMD. Therefore, it results in a smaller NA.  
 210 Secondly, the optimization iteration does not fully converge before being stopped, which is a  
 211 balance between the spatial resolution and the optimization time.

212 After forming a sharp spot behind the diffuser, the optical memory effect can be measured by  
 213 shifting the sample laterally (Fig. 3a). The capillary containing the resin is fixed onto the  
 214 diffuser by a spacer (1 mm). Shifting the diffuser together with the resin is equivalent to  
 215 shifting the beam except that the focal spot will remain at the same position on the image  
 216 captured by the camera, making the inspection easier. Fig. 3b shows that the peak intensity of  
 217 the focal spot decreases with the distance  $\Delta x$  from the original position. For this holographic  
 218 diffuser, the full width at half-maximum (FWHM) of the memory effect range is 16  $\mu\text{m}$ .

### Optical memory effect



### Dynamic focusing



219

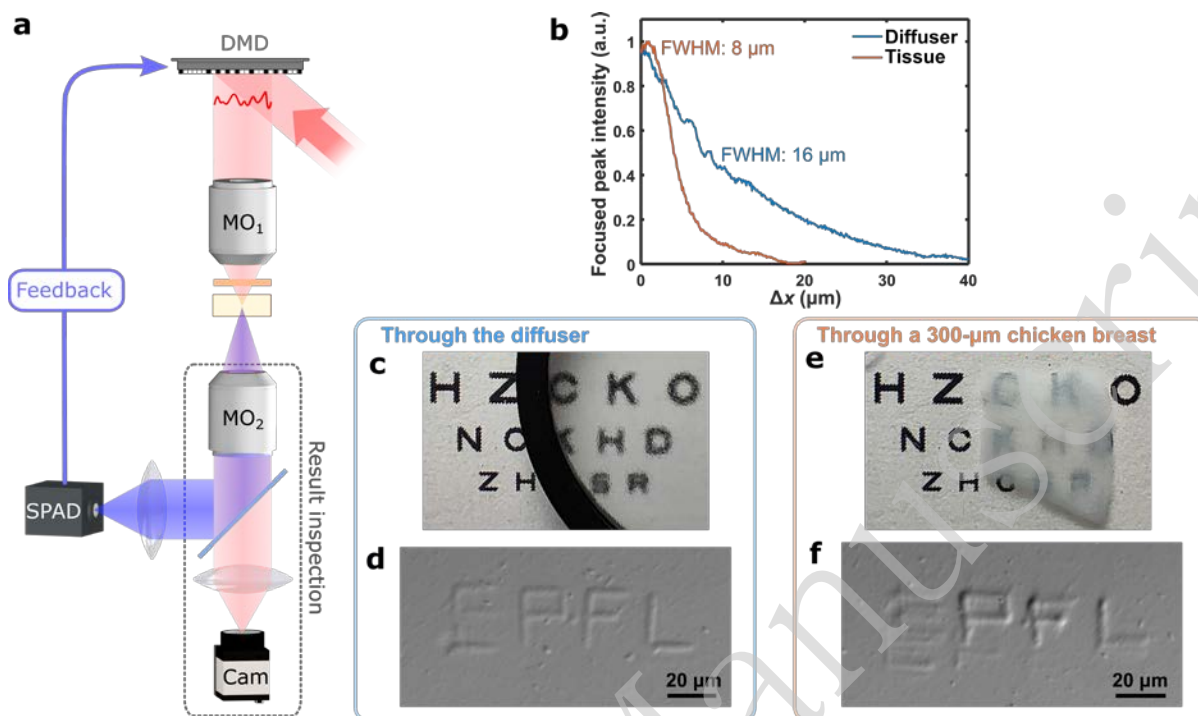
220 **Fig. 3** Dynamic focusing and scanning based on the optical memory effect. **a** Schematic figure of the setup  
 221 showing the lateral shifting of the sample. **b** Focused peak intensity with the DMD pattern from the initial  
 222 focusing versus the shifted distance for the holographic diffuser. Insets show the focal spot at  $\Delta x = 0$  and  $\Delta x =$   
 223 10  $\mu\text{m}$ . FWHM of the focal spot, 1.76  $\mu\text{m}$ . Scale bars, 10  $\mu\text{m}$ . Focused peak intensity versus the shifted distance  
 224 (c) and time (d) during the dynamic focusing. The scanning process results in a decrease in peak intensity at the  
 225 focal spot. The focusing process is repeated every 5  $\mu\text{m}$  to maintain a sharp and intense focus. **e** NIR light dose  
 226 without and with dynamic focusing after a shifted distance of 25  $\mu\text{m}$ . The curve on the right-hand side of each  
 227 image shows the NIR intensity profile along  $\Delta x = 12.5 \mu\text{m}$ .

228 Thanks to the memory effect, we are able to scan the focal spot within the field of view  
229 without changing the DMD pattern at each printed voxel. However, the spot intensity  
230 decreases with the shifting distance, as well as the contrast (Fig. S6), and a high-resolution  
231 structure can only be fabricated within a small area around the initial focusing position. In  
232 addition, the light dose is not uniform, resulting in different degrees of polymerization across  
233 the structure. To maintain a similar light dose at each voxel to be printed, we adopt dynamic  
234 focusing. The focused spot is shifted across the diffuser over 5  $\mu\text{m}$  before the re-focusing  
235 process starts again (Fig. 3c). The optimized pattern from the previous focusing process  
236 serves as the initial pattern for the new optimization, which greatly increases the converging  
237 speed compared to the optimization from scratch<sup>45</sup>. The peak intensity of the first iteration of  
238 the focusing is lower than that of the ending position of the last scanning process (Fig. 3d)  
239 because random deviations are introduced to the initial pattern in order to find the global  
240 maximum. Because of the low fluorescent signal collected, the speed of the focusing process  
241 is limited to the integrating time of the SPAD for each display. A DMD framerate of 300 Hz  
242 is used to ensure that the signal has enough signal-to-noise ratio to reflect the information of  
243 the speckle. The focusing time is approximately 90 s (limited by the fluorescence collection)  
244 and the scanning time is approximately 50 s (limited by the required dose to solidify the resin)  
245 for each 5  $\mu\text{m}$  of lateral shift. The focal spot maintains a relatively stable intensity during the  
246 whole process. Fig. 3e shows the NIR light dose distribution on the focal plane with and  
247 without dynamic focusing. The experiment without dynamic focusing is conducted by  
248 laterally shifting the speckle over the same total distance (25  $\mu\text{m}$ ). The light dose distribution  
249 is calculated by summing up the NIR speckle patterns during the scanning process according  
250 to the shifting distance. The profile at  $\Delta x = 12.5 \mu\text{m}$  is plotted on the right-hand side of each  
251 image to show the contrast. With dynamic focusing, we are able to create a dose distribution  
252 in the shape of a sharp line with a uniform intensity.

253 Invasive printing is first conducted in order to explore the possibilities of this technique in  
254 tissues without the limitation of the low fluorescent signal after back-scattering. It is  
255 demonstrated using both a holographic diffuser and a slice of 300- $\mu\text{m}$ -thick chicken breast.  
256 We call this invasive printing because the SPAD detector is placed on the distal side of the  
257 sample (Fig. 4a). It is worth stressing that this is the only case in this study, in which the  
258 feedback signal is collected in a transmission-based configuration. As the fluorescence is  
259 directly collected from the emission site, and thus not experiencing strong loss due to back-  
260 scattering, the integration time of the SPAD can be significantly decreased, reducing the

261 optimization time down to 20 s (the DMD displays patterns at 1 kHz during the iterative  
262 optimization). The framerate is limited by the long rise time ( $\sim 0.2$  ms) and decay time ( $\sim 0.3$   
263 ms) of the upconverted luminescence of our UCNP (see Section S7, Supplementary  
264 Information). With a faster light modulation, multiple illumination patterns might contribute  
265 to the measured fluorescent signal, resulting in inaccurate feedback. The optical memory  
266 effect of the chicken tissue has a FWHM of  $8 \mu\text{m}$ , smaller than that of the diffuser (Fig. 4b).  
267 Fig. 4c and 4e show qualitatively the impact of scattering on the text readability placed  
268 underneath for the holographic diffuser and the chicken breast layer respectively. Letters  
269 “EPFL” are printed to verify the capability of printing length scale several times the optical  
270 memory lateral shift. During the printing, the focusing process is performed at low NIR  
271 power (to benefit from the non-linearity of the fluorescence signal), and lateral scanning is  
272 performed at high NIR power to ensure that the light dose at the focal spot surpasses the  
273 polymerization threshold. Fig. 4d and 4f show the printed structures imaged by a differential  
274 phase contrast (DPC) microscope<sup>51</sup>, which is used in this study because of the low refractive  
275 index mismatch between the polymerized and unpolymerized hydrogels (see Section S8,  
276 Supplementary Information). The bright and dark edges in the DPC image represent the  
277 distribution of phase change (refractive index mismatch) and its contrast (bright minus dark  
278 intensity) is positively correlated with the strength of phase change, hence the degree of  
279 photopolymerization in this study. The initial focal spot of each letter (top-left corner) is  
280 optimized from scratch (a speckle pattern) and the rest is completed with dynamic  
281 optimization (from a dim focal spot). The printed structure through the holographic diffuser is  
282 relatively uniform, matching the result of the light dose (see the supplementary video).  
283 Looking in detail, the line at the bottom of the letter “E” is detached from the rest of the letter  
284 at the bottom-left corner. This is because we have no control over the position of the focal  
285 spot (global maximum), the position of which happens to switch at this position. For the  
286 printed part through the chicken tissue, over-polymerization can be seen in the letter “P” and  
287 “F”, while optimization did not converge completely when printing the letter “E”. It is very  
288 likely that the non-uniformity of muscle fibers in the chicken breast results in different  
289 scattering properties across the tissue. The tissue structure above the letter “E” is probably  
290 more scattering and requires longer focusing time while the tissue above letters “P” and “F”  
291 is less scattering, resulting in a brighter focal spot and a higher degree of polymerization. To  
292 improve the fidelity in practical applications, the criteria for stopping the optimization  
293 process should be based on the converging speed of the feedback signal, ensuring that a focal  
294 spot is formed in each region. As the optimized feedback signal reflects the intensity of the

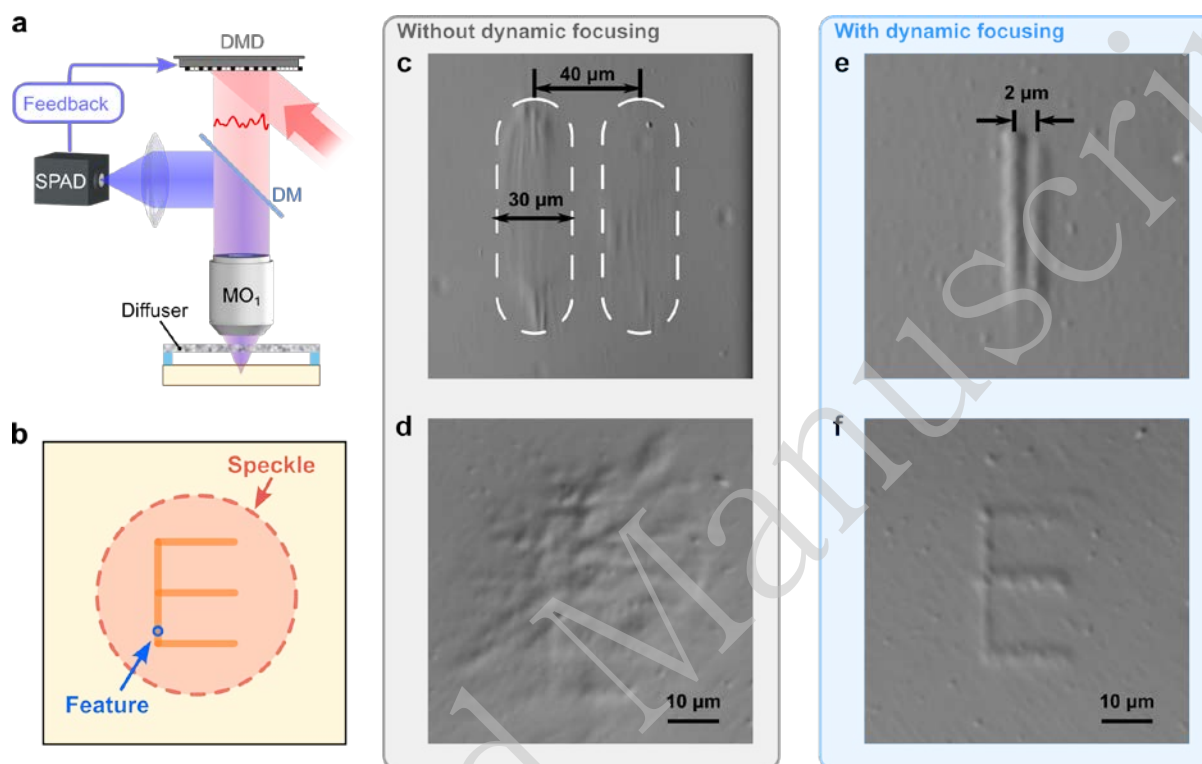
295 focal spot, the laser power for printing can be adjusted in real-time to achieve a similar  
 296 degree of polymerization across the whole structure.



297  
 298 **Fig. 4** Invasive printing. **a** Experimental setup for invasive printing. **b** Focused peak intensity versus shifted  
 299 distance for the holographic diffuser (blue) and for the chicken tissue (orange). Photographs of a target placed  
 300 below the diffuser (**c**) and the tissue (**e**). These scattering media prevent visually differentiating the letters of the  
 301 bottom line. DPC images of printed “EPFL” through the diffuser (**d**) and the tissue (**f**).

302 Non-invasive printing is then demonstrated through the diffuser by placing the SPAD  
 303 detector at the same side as the light delivery (Fig. 5a). The chicken tissue is not tested in this  
 304 configuration: the tissue exhibits excessive scattering at shorter wavelengths, significantly  
 305 decreasing the amount of epi-detected (reflection mode) fluorescence which translates into a  
 306 too-low optimization speed for printing. Based on dynamic focusing, we are able to print fine  
 307 structures within the speckle (Fig. 5b). Without dynamic focusing (DMD acts only as a  
 308 mirror), only hot spots in the speckle are printed. By shifting the sample laterally, lines of  
 309 different contrast and lengths are photopolymerized within the areas highlighted by dash lines  
 310 (Fig. 5c). As the intensity of the speckle grains decreases at the edge of the speckle, there is  
 311 no sharp boundary between the polymerized and unpolymerized area, deteriorating the  
 312 printing fidelity and the printing resolution. The sample is also laterally shifted along the path  
 313 of the letter “E”. As expected, no resolvable structure can be printed inside the speckle size  
 314 without dynamic focusing (Fig. 5d). In contrast, with dynamic focusing, sharp and uniform  
 315 lines with a feature size of  $1.78 \pm 0.39 \mu\text{m}$  (Fig. S8b) can be printed and the minimum

316 resolvable distance that we obtained is  $2\ \mu\text{m}$  (Fig. 5e). Feature size is characterized at 5  
 317 different regions of the structure. Fig. 5f shows a clearly printed letter “E” which is even  
 318 smaller than the speckle size. Although we have no precise control over the absolute position  
 319 of the printing (it may start at any place inside the speckle), the relative position of the  
 320 structures is controlled accurately.



321  
 322 **Fig. 5** Non-invasive printing. **a** Experimental setup for non-invasive printing. **b** Schematic diagram of a  
 323 comparison of the speckle size and the printed feature size. Fine structures can be printed accurately inside the  
 324 speckle. **c** DPC image of two “lines” printed without dynamic focusing and at a distance of  $40\ \mu\text{m}$ . The  
 325 polymerized area is roughly highlighted by white dashed lines because no clear boundary can be observed. **d**  
 326 DPC image of a polymerized part following the path of the letter “E” without dynamic focusing. **e** DPC image  
 327 of two printed lines with a center-to-center distance of  $2\ \mu\text{m}$  using dynamic focusing. **f** DPC image of a printed  
 328 letter “E” using dynamic focusing.

329

## 330 Discussion

331 Focusing light through strongly scattering media had long been considered impossible until  
 332 the recent progress in the field of wavefront shaping. Driven by the ever-growing need for  
 333 deep tissue *in vivo* imaging<sup>30,52</sup>, non-invasive imaging has been achieved through various  
 334 techniques such as blind focusing with nonlinear signals<sup>38,49</sup>, fluorescence-based transmission  
 335 matrix<sup>41,53</sup>, and acoustic manipulation<sup>40</sup>. In this work, we use blind focusing which utilizes

336 nonlinear signals to cope with the issue of low feedback signal. This has been demonstrated  
337 with two-photon imaging<sup>38</sup> and three-photon imaging<sup>46,49</sup> and should be also available for  
338 other nonlinear processes<sup>54</sup>. For linear signals that have enough signal intensities, non-  
339 invasive focusing and imaging can be achieved by collecting the back-scattered fluorescent  
340 patterns<sup>41,53</sup>. Nano-focusing devices<sup>55,56</sup> such as metalens on the end face of a single-mode  
341 fiber have also been proposed for imaging applications. The techniques readily available in  
342 the wavefront shaping might inspire the development of new bioprinting methods against the  
343 turbid nature of the biological tissue.

344 In this work, we make use of an iterative wavefront method to enable non-invasive additive  
345 manufacturing through a scattering layer. The light propagating through the scattering  
346 medium produces complicated speckle patterns that locally excite UCNP. Because of the  
347 nonlinear upconverted fluorescence as the feedback, a sharp focus can be formed in the resin  
348 at a fast optimization speed even with a low signal level. Dynamic focusing is conducted to  
349 ensure a uniform light dose to solidify voxels and combined with the memory effect, the  
350 printing time is optimized. A printing scale 5 times the memory effect size is demonstrated.  
351 Successful printing through a diffuser and a 300- $\mu\text{m}$  chicken tissue proves the feasibility of  
352 this technique. In the non-invasive configuration, we show that a micro-meter resolution  
353 structure can be printed within a speckle pattern that is more than 20 times larger than the  
354 feature size. To the best of our knowledge, this study is the first report on high-resolution  
355 non-invasive printing through a highly scattering medium, which pushes the boundaries of  
356 noninvasive printing to micro-meter resolution.

357 There is much work to be done before the proposed technique can become a tool for non-  
358 invasive *in vivo* printing. Biological tissues are dynamic scattering media<sup>40,57,58</sup> and therefore  
359 the time required to focus light in our approach cannot exceed the ms range. The optimization  
360 speed in the non-invasive focusing is limited by the signal intensity, which can be increased  
361 by using a larger and more sensitive photon detector such as photomultiplier tubes and more  
362 importantly improving the upconversion efficiency of the nanoparticles<sup>59</sup>. SPAD arrays might  
363 also be used to gather the spatial distribution of the fluorescence. Noise-tolerant algorithms  
364 with relatively fast converging speed are preferred and deep learning might also be  
365 implemented for efficient focusing through living tissues<sup>60</sup>. In terms of biocompatibility, the  
366 hydrogels selected in this study are biocompatible and have been widely used in various  
367 biomedical applications<sup>61</sup>. Cell viability experiment of UCNP also indicates their good  
368 cellular compatibility (see Section S9, Supplementary Information).

369 Real applications also pose requirements in the spatial domain. The nature of blind focusing  
370 in this technique denies the possibility of pre-determining the absolute position of the voxel.  
371 In this work, we observe that the global maximum will remain at a hot spot for approximately  
372 25  $\mu\text{m}$  of shifting in the lateral direction before switching to another hot spot within the  
373 illuminated resin. This determines the printing area of one object (see Section S10,  
374 Supplementary Information). The optical memory effect also exists in the axial direction<sup>62</sup>,  
375 indicating the possibility of true 3D printing. As for a larger volume, recent progress in  
376 imaging beyond the memory effect<sup>53</sup> might help to push this boundary. For applications that  
377 require an accurate absolute position of the printed voxels such as connecting the neuron fiber,  
378 feedback with spatial information is necessary.

379 In summary, we have presented a non-invasive additive manufacturing technique to print a  
380 hundred-micron structure size through a strongly scattering medium at micro-meter  
381 resolution based on the fluorescent feedback from the printing system. Thanks to the  
382 nonlinear upconverted fluorescence and the optical memory effect, sub-speckle printing is  
383 demonstrated on a 25- $\mu\text{m}$  size print with a printing resolution of around 2  $\mu\text{m}$ . This technique  
384 provides a promising route toward high-resolution non-invasive bioprinting and shines light  
385 on the development of new techniques for minimally invasive and non-invasive biomedicine.

386

## 387 **Materials and methods**

### 388 **Synthesis of NaYF<sub>4</sub>:Yb/Tm core UCNPs and NaYF<sub>4</sub> shell precursor**

389 Chemicals used in this experiment were purchased from Merck & Co (Sigma-Aldrich) and  
390 the synthesis was carried out in a bifold Schlenk line under the flow of argon gas.

391 In a typical synthesis, thulium (III) acetate hydrate (0.004 mmol) was reacted with oleic acid  
392 (6 mL) and 1-octadecene (15 mL) at 140 °C under partial vacuum having argon atmosphere  
393 for 90 min in a 100 mL 3-neck Schlenk flask to prepare oleate solution. Once the reaction  
394 was complete, first, ytterbium (III) acetate hydrate (0.240 mmol) was reacted with the above  
395 oleate solution for 90 min and afterward, yttrium (III) acetate hydrate (0.556 mmol) was  
396 reacted with this oleate solution at 140 °C. This mixed oleate solution, thus obtained, was  
397 cooled down to 50 °C. To this, methanol solution (10 ml) of ammonium fluoride (3.2 mmol)  
398 and sodium hydroxide (2 mmol) was added dropwise and stirred for 30 min. Methanol was  
399 completely removed under partial vacuum and the reaction mixture was further heated to



300 °C (~10 °C/min) under argon and maintained for 60 min. The reaction was frozen by the addition of cold ethanol and the nanoparticles were collected by centrifugation, redispersed in cyclohexane. This process was repeated thrice, before the product being used as core UCNP (0.5 mol% Tm<sup>3+</sup>, 30 mol% Yb<sup>3+</sup> doped) in the next step.

Similarly, in the second step, yttrium (III) acetate hydrate (0.8 mmol), oleic acid (6 ml) and 1-octadecene (15 ml), methanol solution (10 ml) of ammonium fluoride (4 mmol) and sodium hydroxide (2.5 mmol) were used to prepare the NaYF<sub>4</sub> shell precursor.

#### **Synthesis of ligand free NaYF<sub>4</sub>:Yb/Tm @ NaYF<sub>4</sub> core-shell UCNPs**

Layer-by-layer successive epitaxial shell growth of NaYF<sub>4</sub> was achieved on NaYF<sub>4</sub>:Yb/Tm core UCNPs. Core UCNPs were added to 1-octadecene (5 mL) in a 3-neck Schlenk flask and heated to 300 °C in an argon atmosphere. To this, shell precursor solution was injected @ 5 µL/sec using a Nemesys syringe pump system. The ripening was done at 300 °C for 30 min. After ripening, the reaction was frozen and the core-shell UCNPs were precipitated and washed as outlined for core UCNPs and finally dispersed in hexane (5 mL). These dispersed particles were neutralized using 2M HCl to get the ligand-free core-shell UCNPs.

#### **Synthesis of gelMA**

10 g of gelatin (Sigma-Aldrich) was dissolved in 100 mL of phosphate-buffered saline. Then 8 mL of methacrylic anhydride (Sigma-Aldrich) was added dropwise (0.5 mL/min) and the mixture was left under stirring at 50 °C for 3 hours, followed by removal of unreacted anhydride by centrifugation and dialysis against distilled water. GelMA was obtained after lyophilization.

#### **Preparation of UCNP-loaded hydrogel**

Lithium phenyl-2,4,6-trimethylbenzoyl-phosphinate (LAP) (Sigma-Aldrich) was dissolved in water at a concentration of 20 mg/mL. 10 µL of UCNP aqueous solution (100 mg/mL) was mixed with 50 µL of LAP solution and sonicated for 30 min. 15 mg of gelMA was dissolved in the mixture and 40 µL water was added to form a final concentration of 10 mg/mL UCNP, 10 mg/mL LAP and 15 wt% gelMA. The resin was stored at 4 °C until further use.

A uniform distribution of UCNPs in the resin is a critical factor in focusing and printing. If they are not uniformly distributed or even appear in the form of clusters, the optimized focal spot will always be located at the concentrated region. The distribution of UCNPs in the resin was checked by the fluorescent profile of a collimated 976 nm beam at the transverse plane

431 (Fig. S13). The resin preparation process was optimized to ensure a uniform fluorescent  
432 profile.

### 433 **Characterization**

434 Transmission electron microscopy images were acquired on a Tecnai Osiris electron  
435 microscope, with an accelerating voltage of 200kV. FTIR spectra were recorded by making  
436 KBr pellets of the power samples and measuring them on a Spectrum 3 spectrophotometer  
437 (PerkinElmer). Zeta potential was recorded by Nano ZS (Malvern) using dynamic light  
438 scattering. The UV-Vis spectrum of LAP was recorded on a Lambda 365 UV/Vis  
439 spectrophotometer. The upconverted fluorescence emission spectrum was recorded on a setup  
440 as previously reported<sup>48</sup>. DPC images were recorded on a microscope as previously  
441 reported<sup>51</sup>.

### 442 **Experimental setup**

443 A continuous-wave laser at 976 nm (900 mW, BL976-PAG900, Thorlabs) with a  
444 Polarization-Maintaining (PM) optical fiber is collimated by a lens (F810APC-1064,  
445 Thorlabs). After modulated by the DMD (V-650L, Vialux), the NIR light is directed through  
446 the objective MO<sub>1</sub> (M Plan Apo NIR 20X, NA 0.40, Mitutoyo) to excite the UCNPs in the  
447 resin placed below the scattering medium. The DMD is imaged to the back focal plane of  
448 MO<sub>1</sub>. The scattering medium is a holographic diffuser (Newport 5°) or a slice of fixed  
449 chicken breast. The upconverted fluorescence is back-scattered by the medium, collected by  
450 MO<sub>1</sub> and a lens ( $f = 15$  mm), and detected by a SPAD (PDM-50-CTD, Micro Photon  
451 Devices). We use two longpass dichroic mirrors (DMLP550R, Thorlabs, FF699-FDi01-t1-  
452 25x36, Semrock) and two shortpass filters (FESH0600, Thorlabs and FF01-720/SP-25,  
453 Semrock) to narrow the spectral bandwidth. The NIR speckle patterns are imaged in  
454 transmission via MO<sub>2</sub> (LIO-40X, NA 0.65, Newport) and a lens ( $f = 150$  mm) onto the Cam  
455 (acA2040-55um, Basler). This part of the setup is only used for monitoring the NIR speckles.  
456 In the invasive configuration, the fluorescence is collected in transmission through MO<sub>2</sub> and a  
457 lens (AC254-030-A, Thorlabs), reflected by a longpass dichroic mirror (FF552-Di02-25x36,  
458 Semrock), filtered by two shortpass filters (FESH0600, Thorlabs and FF01-720/SP-25,  
459 Semrock), and detected by the SPAD.

### 460 **Focusing**

461 The optimization was done with the SNES algorithm<sup>50</sup> (see algorithm flow chart in Fig. S11,  
462 Supplementary information). The initial Gaussian parameter  $\mu$  is a random array from [0,1)

463 with a length of segment number and  $\sigma$  is an array of the same length filled with ones. During  
 464 optimization, each segment of DMD is parameterized by  $\mu$  and  $\sigma$ .  $N_{pop}$  grayscale patterns are  
 465 generated according to  $\mu + \sigma s_n$ , where  $s_n$  ( $n = 1, 2, \dots, N_{pop}$ ) is an array with a length of  
 466 segment number and its elements follow the standard normal distribution. Then these  
 467 grayscale patterns are converted to binary patterns via a multi-pixel encoding method<sup>50</sup> and  
 468 displayed by DMD. SPAD is synchronized with DMD to collect total fluorescent signals of  
 469 each binary pattern. After that, all the patterns are sorted according to their power-corrected  
 470 feedback signals in increasing order and multiplied with weights  $u_n$ . The weights for the first  
 471  $N_{pop}/2$  patterns are set to 0 and the rest are set as an arithmetic sequence with a sum of 1. The  
 472 natural gradients for  $\mu$  and  $\sigma$  are calculated by Eq. (2).

$$\begin{cases} \nabla_{\mu} J = \sum_{n=1}^{N_{pop}} u_n \cdot s_n \\ \nabla_{\sigma} J = \sum_{n=1}^{N_{pop}} u_n \cdot (s_n^2 - 1) \end{cases} \quad (2)$$

473 The updated  $\mu$  and  $\sigma$  are calculated by Eq. (3).

$$\begin{cases} \mu_{i+1} = \mu_i + \eta_{\mu} \sigma_i \cdot \nabla_{\mu} J \\ \sigma_{i+1} = \sigma_i \exp\left(\frac{\eta_{\sigma}}{2} \nabla_{\sigma} J\right) \end{cases} \quad (3)$$

474  $\eta_{\mu}$  and  $\eta_{\sigma}$  are the learning rates for  $\mu$  and  $\sigma$ , respectively. In this study, we set  $\eta_{\mu} = 1$  and  
 475  $\eta_{\sigma} = 0.08$ . The segment number is  $32 \times 17$  and the segment size is  $25 \times 50$ , which means that a  
 476 range of  $800 \times 850$  pixels on the DMD is used for light modulation. The light distribution on  
 477 DMD was calibrated by sequentially turning on each segment and measuring the difference  
 478 in the output power. In each segment, the number of encoded pixels is 5, and the coding  
 479 strategy is as previously reported<sup>50</sup>. It is encoded in the  $x$ -axis and expanded to the size of a  
 480 segment by repeating each pixel in the  $x$ - and  $y$ -axis (see Section S4, Supplementary  
 481 information). The population size is 40 and the iteration is 200 for invasive focusing and 400  
 482 for non-invasive focusing. These parameters are chosen to balance the optimization speed  
 483 and the enhancement (see Section S12, Supplementary information). The DMD display speed  
 484 is mainly limited by the fluorescent signal intensity. 1 kHz is used in the invasive  
 485 configuration and 200~300 Hz is used in the non-invasive configuration.

## 486 **Printing**

487 The UCNP-loaded hydrogel was sonicated at 40 °C for 1 min before it was filled into the  
 488 rectangular capillary ( $20 \mu\text{m} \times 200 \mu\text{m}$ , CM Scientific). The capillary was fixed onto the

489 diffuser, which was pasted on a glass slide in order to be clamped by the sample holder. The  
490 distance between the holographic diffuser and the resin is 1 mm in air and 14  $\mu\text{m}$  of capillary  
491 glass wall; the distance between the chicken tissue and the resin is 170  $\mu\text{m}$  of the coverslip  
492 and 14  $\mu\text{m}$  of the glass wall. A “white” pattern was displayed on the DMD, making it just as  
493 a mirror. The sample was aligned in the  $x$ ,  $y$ , and  $z$  direction so that the capillary is  
494 illuminated by the speckle and the speckle size within the capillary is about 30~50  $\mu\text{m}$ . Then  
495 the SPAD was aligned to maximize the fluorescent signal.

496 During the printing, the focusing process was conducted at low power (~7 mW before  $\text{MO}_1$ ),  
497 and then the focal spot was scanned at higher power (~25 mW before  $\text{MO}_2$ ) in order to  
498 surpass the polymerization threshold. The hatching distance is 1  $\mu\text{m}$  and the scanning speed  
499 is 0.1  $\mu\text{m}/\text{s}$ .

500 UCNPs exhibit stable optical response during 1-hour illumination of 976 nm light (Fig. S14),  
501 indicating their reliable performance during printing.

## 502 **Tissue fixation**

503 A piece of fresh chicken breast was cut into 4-mm cubes and fixed with 10% buffered  
504 formalin (HT501128-4L, Sigma Aldrich) overnight. Then the fixed samples were rinsed in  
505 phosphate-buffered saline three times and embedded in 2% agarose until solidified. The  
506 embedded tissues were cut into 300- $\mu\text{m}$ -thick slices using a vibratome (VT1200 S, Leica),  
507 and mounted onto glass slides (Sigma-Aldrich) with Fluoromount-G (SouthernBiotech). 300-  
508  $\mu\text{m}$  spacers were used to confine specimens without compression. The sections were sealed  
509 with nail polish and kept at 4 °C for 24 hours before being used for printing.

510

## 511 **Acknowledgment**

512 This project has received funding from the Swiss National Science Foundation under project  
513 number 196971 - “Light based Volumetric printing in scattering resins.” The authors thank  
514 the open-source tools (and their contributors) that were used in this work, including  
515 Inkscape.org, Python.org, and Fiji.sc. The authors would like to acknowledge Dr. Jessica  
516 Sordet-Dessimoz (Histology Core Facility, EPFL) for assistance with tissue sectioning. The  
517 authors would like to acknowledge Dr. David Fernando Reyes Vasquez (Interdisciplinary  
518 Centre for Electron Microscopy, EPFL) for assistance with transmission electron microscopy.

519 The authors also acknowledge Dr. Yann Lavanchy (Molecular and Hybrid Materials  
520 Characterization Center, EPFL) for assistance with FTIR and Zeta-potential characterization.

521

## 522 **Conflict of interest**

523 The authors declare no conflicts of interest regarding this article.

524

## 525 **Reference**

- 526 1. Moroni, L. et al. Biofabrication strategies for 3D in vitro models and regenerative  
527 medicine. *Nature Reviews Materials* **3**, 21-37 (2018).
- 528 2. Murphy, S. V., De Coppi, P. & Atala, A. Opportunities and challenges of translational 3D  
529 bioprinting. *Nature Biomedical Engineering* **4**, 370-380 (2020).
- 530 3. Lee, A. et al. 3D bioprinting of collagen to rebuild components of the human heart.  
531 *Science* **365**, 482-487 (2019).
- 532 4. De Santis, M. M. et al. Extracellular-matrix-reinforced bioinks for 3D bioprinting human  
533 tissue. *Advanced Materials* **33**, 2005476 (2021).
- 534 5. You, S. T. et al. High cell density and high-resolution 3D bioprinting for fabricating  
535 vascularized tissues. *Science Advances* **9**, eade7923 (2023).
- 536 6. Daly, A. C. et al. 3D bioprinting of high cell-density heterogeneous tissue models  
537 through spheroid fusion within self-healing hydrogels. *Nature Communications* **12**, 753  
538 (2021).
- 539 7. Qiu, B. N. et al. Bioprinting neural systems to model central nervous system diseases.  
540 *Advanced Functional Materials* **30**, 1910250 (2020).
- 541 8. Nie, J. et al. Grafting of 3D bioprinting to in vitro drug screening: a review. *Advanced*  
542 *Healthcare Materials* **9**, 1901773 (2020).
- 543 9. Janani, G. et al. Mimicking native liver lobule microarchitecture in vitro with parenchymal  
544 and non-parenchymal cells using 3D bioprinting for drug toxicity and drug screening  
545 applications. *ACS Applied Materials & Interfaces* **14**, 10167-10186 (2022).
- 546 10. Matai, I. et al. Progress in 3D bioprinting technology for tissue/organ regenerative  
547 engineering. *Biomaterials* **226**, 119536 (2020).
- 548 11. Li, X. D. et al. Inkjet bioprinting of biomaterials. *Chemical Reviews* **120**, 10793-10833  
549 (2020).
- 550 12. Zhang, Y. S. et al. 3D extrusion bioprinting. *Nature Reviews Methods Primers* **1**, 1-20  
551 (2021).
- 552 13. Chang, J. L. & Sun, X. M. Laser-induced forward transfer based laser bioprinting in  
553 biomedical applications. *Frontiers in Bioengineering and Biotechnology* **11**, 1255782  
554 (2023).
- 555 14. Li, W. L. et al. Stereolithography apparatus and digital light processing-based 3D  
556 bioprinting for tissue fabrication. *iScience* **26**, 106039 (2023).
- 557 15. Bernal, P. N. et al. Volumetric bioprinting of organoids and optically tuned hydrogels to  
558 build liver-like metabolic biofactories (Adv. Mater. 15/2022). *Advanced Materials* **34**,  
559 2270112 (2022).
- 560 16. Lee, M. et al. Guiding lights: tissue bioprinting using photoactivated materials. *Chemical*  
561 *Reviews* **120**, 10950-11027 (2020).
- 562 17. Miri, A. K. et al. Effective bioprinting resolution in tissue model fabrication. *Lab on a Chip*  
563 **19**, 2019-2037 (2019).

- 564 18. Chae, S. & Cho, D. W. Biomaterial-based 3D bioprinting strategy for orthopedic tissue  
565 engineering. *Acta Biomaterialia* **156**, 4-20 (2023).
- 566 19. Heinrich, M. A. et al. 3D bioprinting: from benches to translational applications. *Small* **15**,  
567 1805510 (2019).
- 568 20. Singh, S. et al. *In situ* bioprinting – Bioprinting from benchside to bedside? *Acta*  
569 *Biomaterialia* **101**, 14-25 (2020).
- 570 21. Xie, M. J. et al. In situ 3D bioprinting with bioconcrete bioink. *Nature Communications* **13**,  
571 3597 (2022).
- 572 22. Chen, Y. W. et al. Noninvasive in vivo 3D bioprinting. *Science Advances* **6**, eaba7406  
573 (2020).
- 574 23. Urciuolo, A. et al. Intravital three-dimensional bioprinting. *Nature Biomedical*  
575 *Engineering* **4**, 901-915 (2020).
- 576 24. Karami, P. et al. NIR light-mediated photocuring of adhesive hydrogels for noninvasive  
577 tissue repair via upconversion optogenesis. *Biomacromolecules* **23**, 5007-5017 (2022).
- 578 25. Zhou, C. et al. Ferromagnetic soft catheter robots for minimally invasive bioprinting.  
579 *Nature Communications* **12**, 5072 (2021).
- 580 26. Jacques, S. L. Optical properties of biological tissues: a review. *Physics in Medicine &*  
581 *Biology* **58**, R37-R61 (2013).
- 582 27. Zong, W. J. et al. Miniature two-photon microscopy for enlarged field-of-view, multi-  
583 plane and long-term brain imaging. *Nature Methods* **18**, 46-49 (2021).
- 584 28. Wan, H. et al. Molecular imaging in the second near-infrared window. *Advanced*  
585 *Functional Materials* **29**, 1900566 (2019).
- 586 29. Li, C. Y. et al. Advanced fluorescence imaging technology in the near-infrared-II window  
587 for biomedical applications. *Journal of the American Chemical Society* **142**, 14789-  
588 14804 (2020).
- 589 30. Chen, L. L. et al. Near-infrared-II quantum dots for in vivo imaging and cancer therapy.  
590 *Small* **18**, 2104567 (2022).
- 591 31. Huo, M. F. et al. Upconversion nanoparticles hybridized cyanobacterial cells for near-  
592 infrared mediated photosynthesis and enhanced photodynamic therapy. *Advanced*  
593 *Functional Materials* **31**, 2010196 (2021).
- 594 32. Lv, Z. Q. et al. Noble metal nanomaterials for NIR-triggered photothermal therapy in  
595 cancer. *Advanced Healthcare Materials* **10**, 2001806 (2021).
- 596 33. Kiefer, P. et al. Sensitive photoresists for rapid multiphoton 3D laser micro- and  
597 nanoprinting. *Advanced Optical Materials* **8**, 2000895 (2020).
- 598 34. Chen, Z. J. et al. Near-infrared light driven photopolymerization based on photon  
599 upconversion. *ChemPhotoChem* **3**, 1077-1083 (2019).
- 600 35. Vellekoop, I. M. & Mosk, A. P. Focusing coherent light through opaque strongly  
601 scattering media. *Optics Letters* **32**, 2309-2311 (2007).
- 602 36. Vellekoop, I. M. & Mosk, A. P. Phase control algorithms for focusing light through turbid  
603 media. *Optics Communications* **281**, 3071-3080 (2008).
- 604 37. Yaqoob, Z. et al. Optical phase conjugation for turbidity suppression in biological  
605 samples. *Nature Photonics* **2**, 110-115 (2008).
- 606 38. Katz, O. et al. Noninvasive nonlinear focusing and imaging through strongly scattering  
607 turbid layers. *Optica* **1**, 170-174 (2014).
- 608 39. Horstmeyer, R., Ruan, H. W. & Yang, C. Guidestar-assisted wavefront-shaping methods  
609 for focusing light into biological tissue. *Nature Photonics* **9**, 563-571 (2015).
- 610 40. Liu, Y. et al. Optical focusing deep inside dynamic scattering media with near-infrared  
611 time-reversed ultrasonically encoded (TRUE) light. *Nature Communications* **6**, 5904  
612 (2015).
- 613 41. Boniface, A., Dong, J. & Gigan, S. Non-invasive focusing and imaging in scattering  
614 media with a fluorescence-based transmission matrix. *Nature Communications* **11**, 6154  
615 (2020).
- 616 42. Osnabrugge, G. et al. Generalized optical memory effect. *Optica* **4**, 886-892 (2017).
- 617 43. Judkewitz, B. et al. Translation correlations in anisotropically scattering media. *Nature*  
618 *Physics* **11**, 684-689 (2015).

- 619 44. Yang, X., Pu, Y. & Psaltis, D. Imaging blood cells through scattering biological tissue  
620 using speckle scanning microscopy. *Optics Express* **22**, 3405-3413 (2014).
- 621 45. Wang, X. D. et al. Efficiently scanning a focus behind scattering media beyond memory  
622 effect by wavefront tilting and re-optimization. *Optics Express* **31**, 32287-32297 (2023).
- 623 46. Rauer, B. et al. Scattering correcting wavefront shaping for three-photon microscopy.  
624 *Optics Letters* **47**, 6233-6236 (2022).
- 625 47. Osnabrugge, G., Amitonova, L. V. & Vellekoop, I. M. Blind focusing through strongly  
626 scattering media using wavefront shaping with nonlinear feedback. *Optics Express* **27**,  
627 11673-11688 (2019).
- 628 48. Zhang, Q. Y. et al. Multi-photon polymerization using upconversion nanoparticles for  
629 tunable feature-size printing. *Nanophotonics* **12**, 1527-1536 (2023).
- 630 49. Berlage, C. et al. Deep tissue scattering compensation with three-photon F-SHARP.  
631 *Optica* **8**, 1613-1619 (2021).
- 632 50. Yang, J. M. et al. Anti-scattering light focusing by fast wavefront shaping based on multi-  
633 pixel encoded digital-micromirror device. *Light: Science & Applications* **10**, 149 (2021).
- 634 51. Bonati, C. et al. Lock-in incoherent differential phase contrast imaging. *Photonics*  
635 *Research* **10**, 237-247 (2022).
- 636 52. Yoon, S. et al. Deep optical imaging within complex scattering media. *Nature Reviews*  
637 *Physics* **2**, 141-158 (2020).
- 638 53. Zhu, L. et al. Large field-of-view non-invasive imaging through scattering layers using  
639 fluctuating random illumination. *Nature Communications* **13**, 1447 (2022).
- 640 54. Hahn, V. et al. Challenges and opportunities in 3D laser printing based on (1 + 1)-  
641 photon absorption. *ACS Photonics* **10**, 24-33 (2023).
- 642 55. Kim, M. et al. Deep sub-wavelength nanofocusing of UV-visible light by hyperbolic  
643 metamaterials. *Scientific Reports* **6**, 38645 (2016).
- 644 56. Ren, H. R. et al. An achromatic metafiber for focusing and imaging across the entire  
645 telecommunication range. *Nature Communications* **13**, 4183 (2022).
- 646 57. Luo, J. W. et al. High-speed single-exposure time-reversed ultrasonically encoded  
647 optical focusing against dynamic scattering. *Science Advances* **8**, eadd9158 (2022).
- 648 58. Cheng, Z. T. et al. High-gain and high-speed wavefront shaping through scattering  
649 media. *Nature Photonics* **17**, 299-305 (2023).
- 650 59. Wen, S. H. et al. Advances in highly doped upconversion nanoparticles. *Nature*  
651 *Communications* **9**, 2415 (2018).
- 652 60. Gigan, S. et al. Roadmap on wavefront shaping and deep imaging in complex media.  
653 *Journal of Physics: Photonics* **4**, 042501 (2022).
- 654 61. Yue, K. et al. Synthesis, properties, and biomedical applications of gelatin methacryloyl  
655 (GelMA) hydrogels. *Biomaterials* **73**, 254-271 (2015).
- 656 62. Katz, O., Small, E. & Silberberg, Y. Looking around corners and through thin turbid  
657 layers in real time with scattered incoherent light. *Nature Photonics* **6**, 549-553 (2012).